Martensite and nanobainite transformations in a low alloyed steel studied by in situ high energy synchrotron diffraction

Steve Gaudez, Julien da Costa Teixeira, Sabine Denis, Guillaume Geandier, Sébastien Y.P. Allain

Martensite and nanobainite transformations in a low alloyed steel studied by in situ high energy synchrotron diffraction

Steve Gaudez [1,*], Julien Teixeira [1,2], Sabine Denis [1,2], Guillaume Geandier [1], Sébastien Y.P. Allain [1,2]

[1] Université de Lorraine, CNRS, IJL, F-54000 Nancy, France; [2] Labex DAMAS "Design of Alloy Metals for Low-mass Structures", Université de Lorraine, France

Correspondence: * steve.gaudez@polytechnique.edu

Keywords: diffraction; phase transformation; austenite; dislocation density; carbon mass balance

Abstract Martensitic and nanobainite transformations are studied in situ in a low alloyed, high-Si steel by using in situ HEXRD, combined with dilatometry and SEM observations, and by considering the same steel composition and austenitization conditions. The martensitic microstructure presents a mixed lath-plate morphology with large scatter of sizes whereas the bainite microstructure shows finer laths with more uniform sizes. Recently introduced methods are used to track in situ by HEXRD, in one single experiment, the phase fractions, the distribution of the carbon and the evolution of the dislocation densities. The study of nanobainite revealed that about two thirds of the carbon partitions from the ferrite to precipitate into transition iron carbides or to enrich the austenite. Both processes occur very fast after the formation of each nanobainite lath, but the ferrite remains largely supersaturated in carbon. The dislocation density increases inside each new forming bainitic ferrite lath. It then decreases when recovery becomes preponderant, as described with a recovery model from the literature. After the martensitic transformation, the retained austenite ends up with high hydrostatic compressive stresses. Dislocation densities are higher than in nanobainite and probably more heterogeneous, because recovery is less significant. No carbides were detected, contrary to the nanobainite. The carbon mass balance is analyzed in the light of these new results and previous investigations on similar systems.

1 Introduction

Third generation of advanced high strength steels are designed with composite microstructures composed of high strength phases (e.g. bainite or martensite) and a high fraction of a softer phase (e.g. austenite) in order to optimize the strength/ductility trade-off. Large fractions of retained austenite can be obtained in the microstructure by adding silicon to the steel composition (about 1-2 wt.%), in order to hinder carbides precipitation and thereby stabilize the austenite by carbon enrichment. This led to new concepts, such as e.g. carbide-free-bainite [1], nanobainite [2,3] or Q&P (Quenching and Partitioning) [4] steels and microstructures. As the mechanical properties and the microstructures depend on the thermal treatments, many studies aim at understanding the phase transformation mechanisms. This regards in particular the nanobainite transformation and the martensitic transformation.

Nanobainite microstructures are obtained by austempering at low temperature (ca. 250-300°C) and for duration going up to several days [2,5]. The resulting microstructures consist of fine bainitic ferrite laths (few tens of nm thick) and a large amount of retained austenite (up to about 40%) enriched and stabilized by carbon released by the ferrite. The bainitic ferrite laths show heterogenous dislocation densities, which increase with the progression of the nanobainite transformation [6–8]. Several studies report the precipitation of transition iron carbides and sometimes cementite [3,9], showing that the nanobainite microstructures are in an advanced stage of tempering. Despite the partition of carbon to austenite and the formation of carbides, the bainitic ferrite remains largely supersaturated in carbon, compared to paraequilibrium, even after a long time of treatment as shown by XRD and APT (e.g. [10]).

Martensitic microstructures are very different from nanobainite. Plate and lath sizes are more heterogeneous. Dislocation densities increase with the progression of the martensitic transformation [11,12], like in nanobainite. However, the dislocation densities are higher in martensite than in nanobainite. This could be due to a higher fraction of martensite (last formed martensite having higher dislocation density), and because recovery has more time to occur during austempering of long duration. Even if some autotempering occurs during the cooling

(even for very high cooling rates [13]), the degree of tempering is much less advanced than in nanobainite. It is thus frequently considered that martensitic and retained austenite phases keep the initial carbon composition of the austenite at high temperature, while carbides precipitation is considered negligible. Nevertheless, common features are shared between martensitic and nanobainitic microstructures. In both, carbon remains in supersaturation in solid solution within the bainitic ferrite/martensite (but with higher supersaturation in martensite than in nanobainite). Carbon segregation along linear and planar defects (dislocations, interfaces) and carbon clusters were reported [3, 6, 9, 13, 14].

Several important features of both nanobainitic and martensitic microstructures remain difficult to estimate. First one regards the distribution of the carbon in the microstructure. Knowing this distribution is necessary to understand the phase transformation mechanisms. It also influences the mechanical behavior (solid solution/carbides strengthening) and how the microstructure will evolve during further treatment, especially tempering [14–17]. As mentioned above, some carbon partitions to the austenite, whereas the bainitic ferrite may remain supersaturated in carbon. Another part may segregate to defects, or contribute to carbides precipitation. Some studies have tried to understand where the carbon is located in the microstructure by trying to achieve a carbon mass balance in martensite [18] and nanobainite [3, 19] respectively through synchrotron X-ray diffraction and combination of high energy X-ray diffraction (HEXRD), transmission electron microscopy and atom probe tomography (APT). In both nanobainite and martensitic microstructures, the carbon mass balance could in most cases not be fully achieved. Except in [3], a significant "carbon-deficit" is reported in these studies. The reason is that it remains difficult to estimate the carbon content at each location in the microstructure. For instance, the carbon concentration in solid solution in the bainitic ferrite/martensitic phases is frequently estimated from the tetragonal ratio of the cell parameters, but the corresponding proportionality relationship is not yet fully established [13, 20–22]. This is also the case for the reported stoichiometry of the transition iron-carbides, which ranges between Fe_3C and Fe_2C [4, 23] according to APT observations. The stoichiometry could also be influenced by the amount of Si in the steel [24]. Finally, there are also large uncertainties regarding the amount of carbon segregated to defects (e.g. [19]).

Second microstructural feature of interest for both microstructures is the dislocation density, because of its direct influence on the mechanical behavior and because the carbon segregates to these defects. Dislocation densities in martensite have been investigated by XRD and by TEM observations [25–27]. Recently, an in situ XRD method has been introduced in [12]. It is based on a Williamson-Hall analysis [28, 29] of the diffraction peaks, allowing to estimate the evolution of the dislocation density in the martensite and in the austenite during the cooling. It came out that the dislocation densities in martensite are highly heterogeneous. During the cooling, each new martensite plate-lath forms with increasing dislocation density. Meanwhile, the austenite work-hardens due to the plastic accommodation of the phase transformations strains. Dislocation densities have also been investigated in the case of nanobainite transformation [3, 6, 7, 30]. In [6, 7, 12]; it is suggested that the increase of the dislocation density with the progression of the phase transformation comes from the work hardening of the austenite. The bainitic ferrite or the martensite may inherit some part of the dislocations structure of the austenite. The formation of bainitic ferrite or martensite in a harder matrix is another possible origin.

In this article, experimental analyses based on in situ synchrotron HEXRD recently introduced to study martensitic and nanobainite transformations are combined to follow, in one single experiment, the dislocation densities and the carbon mass balance, together with the phase transformation kinetics. A first attempt to follow the dislocation density evolutions during a nanobainite transformation will be presented (in addition to already investigated case of martensitic transformation [12]). The impact of the carbon segregation to dislocations on the carbon mass balance will be quantified. Thanks to a precise carbon mass balance, new insight will be given regarding two issues: the redistribution of the carbon upon nanobainite transformation and the supersaturation of the carbon, both in nanobainitic ferrite or martensitic plates/laths. These analyses will be complemented by dilatometry experiments and SEM observations.

2 Material and methods

The investigated steel composition is given in Table 1. The composition was measured by optical emission spectrometry for substitutional elements and by infrared spectrometry for carbon. The maximum uncertainty

in carbon concentration for this technique is close to 0.01%. A 20 kg ingot was produced by Ascometal (Hagondange, France) by vacuum induction melting, hot forged at 1250°C in a 40 mm square cross section bar and finally softened for 16 h at 720°C followed by air-cooling to room temperature. The as-softened microstructure presents globular carbides surrounded by ferrite, which are visible at the optical microscope scale. Carbides present within the microstructure were identified by high energy X-ray diffraction and are cementite and MC-type (FCC) carbides. Samples were machined parallel to the bar length at mid radius to avoid the macro-segregations at the surface and in the center. The samples were austenitized at 1150°C during three minutes after a continuous heating at 5°C/s. This high temperature was required to dissolve primary carbides according to thermodynamic calculations and as it was confirmed experimentally by in situ HEXRD. This austenitization treatment led to a mean prior austenite grain size of 60.6±29 μm revealed by thermal etching [31].

Three thermal treatments are considered:

- Nanobainite formed by austempering during 20 hours at 250°C followed by gas quench (continuous cooling from 1150°C to 250°C at 5°C/s prevented any prior decomposition of austenite),
- Martensite + retained austenite obtained by gas quenching from 1150°C to room temperature,
- Martensite obtained by quenching in liquid nitrogen in order to continue the martensite transformation and thus reduce the retained austenite phase fraction.

The three microstructures will be denoted LNM, RTM and NB respectively for Liquid Nitrogen quenched Martensite, Room Temperature quenched Martensite and NanoBainite.

Table 1: Steel composition in weight percent.

Elt.	C	Cr	Mn	Si	Mo	V	Ni	Cu	Fe
wt.%	0.67	1.73	1.32	1.67	1.0	0.5	0.2	0.18	Bal.

The thermal treatments were performed with an in-house vertical dilatometer designed for fast thermal cycles under primary vacuum (5×10^{-4} mbar) with a 3 mm diameter and 30 mm length sample size. Fast heating and cooling is achieved by radiation heating (with lamps) and by helium gas blowing down to 250°C, followed by pressurized air down to room temperature. Further cooling down to the liquid nitrogen temperature was achieved by plunging the sample into liquid nitrogen during five minutes to decrease the temperature down to ca. -196°C. During the thermal treatment, the temperature is followed thanks to a K-type thermocouple spot welded at the half-length of the sample. The relative displacement is measured by a linear voltage differential transducer (LVDT) and quartz push-hollow rods.

High energy X-ray diffraction experiments were performed at the Deutsches Elektronen Synchrotron (DESY) in Hamburg, Germany on the PETRA III P07 beamline which was configured in transmission mode with a monochromatic beam of 100 keV ($\lambda = 0.123984$ Å). An LaB_6 standard reference was used to obtain the instrumental broadening which was assumed constant during the experiments. The diffracted Debye-Scherrer rings were collected continuously during the thermal treatment thanks to a 2D Perkin Elmer XRD 1621 Flat Panel detector located at ca. 1.5 m away from the sample giving access to full Debye Scherrer ring up to 8 $2\theta(°)$. Two frequencies were used: 10 images/s for the fast martensite transformation and 1 image/min for the nanobainite transformation. The thermal treatments were performed with a dilatometer installed on the beamline (modified Bahr DIL 805 A/D). Only RTM and NB microstructures were investigated in situ by HEXRD, as martensitic transformation down to the liquid nitrogen temperature could not be followed with the experimental setup. The Debye-Scherrer rings collected on the 2D detector were continuous, showing that powder diffraction conditions were achieved. They were integrated circularly with the pyFAI Python library [32] to obtain intensity/2θ diagrams. Rietveld analysis of 1D diagrams was performed with the FullProf software [33]. Three crystal systems are considered: body centered tetragonal phase (I4/mmm) corresponding to martensite and bainitic ferrite, cubic face centered (Fm-3m) for austenite and orthorhombic for transition-carbides (Pnnm). No clear distinction can be made between ϵ (hexagonal $P6_322$) [14] and η (orthorombic Pnnm) [34] carbides, as it was also concluded in [35–37] from TEM and XRD investigations. Considering ϵ or η iron carbide(s) during the analysis did not change the main trends. The phase fractions were affected below the experimental resolution.

It was chosen to use the η carbide crystal structure for the Rietveld analyses, and to consider it as representative of the transition-carbides, whatever their actual crystallographic structure. These will hereafter be denoted TCs.

The dislocation densities in the bainitic ferrite or in the martensitic phase were investigated by using the Williamson-Hall (WH) method, which relates the Full Width Half Maximum (FWHM) and the position of the diffraction peaks to the microstrains and the crystallite sizes. The classical WH method [28] was improved to a modified Williamson-Hall method (mWH), which takes account of the consequence of the anisotropic elasticity [29]. After some simplification [38], the peak width ΔK reads:

$$\Delta K = \frac{0.9}{D} + \sqrt{\frac{\pi M_d b^2}{2}} K_{hkl} \sqrt{\rho \overline{C}_{hkl}} \tag{1}$$

where ΔK is the peak width expressed as $0.5\,\mathrm{FWHM}(\theta) \cdot 2\cos(\theta)/\lambda$, with θ the diffraction angle and λ the wavelength. D is the crystallite size, b the magnitude of the Burgers vector 2.55 Å, K_{hkl} the magnitude of diffraction vector equal to $2\sin(\theta)/\lambda$, ρ the dislocation density. M_d is a dimensionless parameter linked to the dislocation density and the outer cutoff radius. It is considered constant and set to 2.5, as justified in [39]. $\overline{C}_{hkl}$ is the average dislocation contrast factor. The contrast factors were calculated from [40] (see also [41]), considering ferrite elastic constants $C_{11} = 231.5$, $C_{12} = 135.0$ and $C_{44} = 116.0$ GPa. The proportion of edge and screw dislocations influences the alignment of the couples $K^2C - \Delta K$ of the modified Williamson-Hall method used. The best alignment compromise for the three microstructures and all along the thermal treatments was obtained assuming equal density of edge and screw dislocations. Proportion of each dislocation type is hard to estimate experimentally and is often assumed constant and set to 0.5 [29,42,43]. Assuming different proportions (e.g. 100 % screw or 100 % edge) has a limited effect on the dislocation density calculated in this work and does not affect the trend observed during transformations. Thus, it was assumed an equal density of edge and screw dislocations in $\{110\}\langle 111\rangle$ slip system. For the reticular planes considered in the mWH analysis, the contrast factors are equal to 0.283 for {200}, 0.232 for {310} and 0.141 for {211}, {220} and {312}. Further details about the dislocation density measurement can be found in [12] and [39].

Finally, samples were cut in half and ground to perform hardness measurements. The Vickers hardness tests were realized with a 30 kg load, averaging both lengths of the square diagonals and performing for each treatment five measurements sufficiently spaced out with each other. The other sample parts were ground up to a mirror polishing (SiC sand paper up to 4000 followed by diamond polishing from 3 to 1 μm and silica suspension). They were then etched with a nital 2% solution. The microstructures were investigated by scanning electron microscopy with a FEI Quanta 650 FEG.

3 Results

3.1 Microstructure

The three considered microstructures were observed by scanning electron microscopy (Figure 1). In both martensite microstructures (LNM and RTM), plates and laths morphologies are visible, as expected from the carbon content of the steel [17]. A large distribution of sizes is visible in the micrographs. Largest plates contain midribs, which consist of heavily twinned center lines [44]. For the NB microstructure, the thicknesses of the bainitic ferrite laths are more uniform. Retained austenite is visible with two morphologies: in films between bainite laths (bright contrast) and in blocks between bainite sheaves (dark contrast with bright layer at boundaries).

The plates-laths thickness distributions were measured from the SEM micrographs. These were measured in a line perpendicular to the long dimension of the plates-laths. A stereological correction was then applied, because the observations were done in random sections. The true plate-lath thickness t is given by [45]:

$$t = \frac{2}{\pi} L_T \tag{2}$$

where L_T is the thickness measured in the plane of observation and perpendicular to the long direction of the plate-lath.

Figure 1 shows the size distributions, which are well represented by a log-normal fit. In both martensites, there is a large distribution of plate-lath widths. As expected, the average size is lower in LNM (209±145 nm) than in RTM microstructure (354±225 nm), because of the formation of thinner plates-laths during the quench into liquid nitrogen. (The dispersion around the average value corresponds to one standard deviation of the log-normal fits). Conversely, the size distribution is much more homogeneous for the NB microstructure (formed in isothermal condition) with a mean lath size of 87±34 nm.

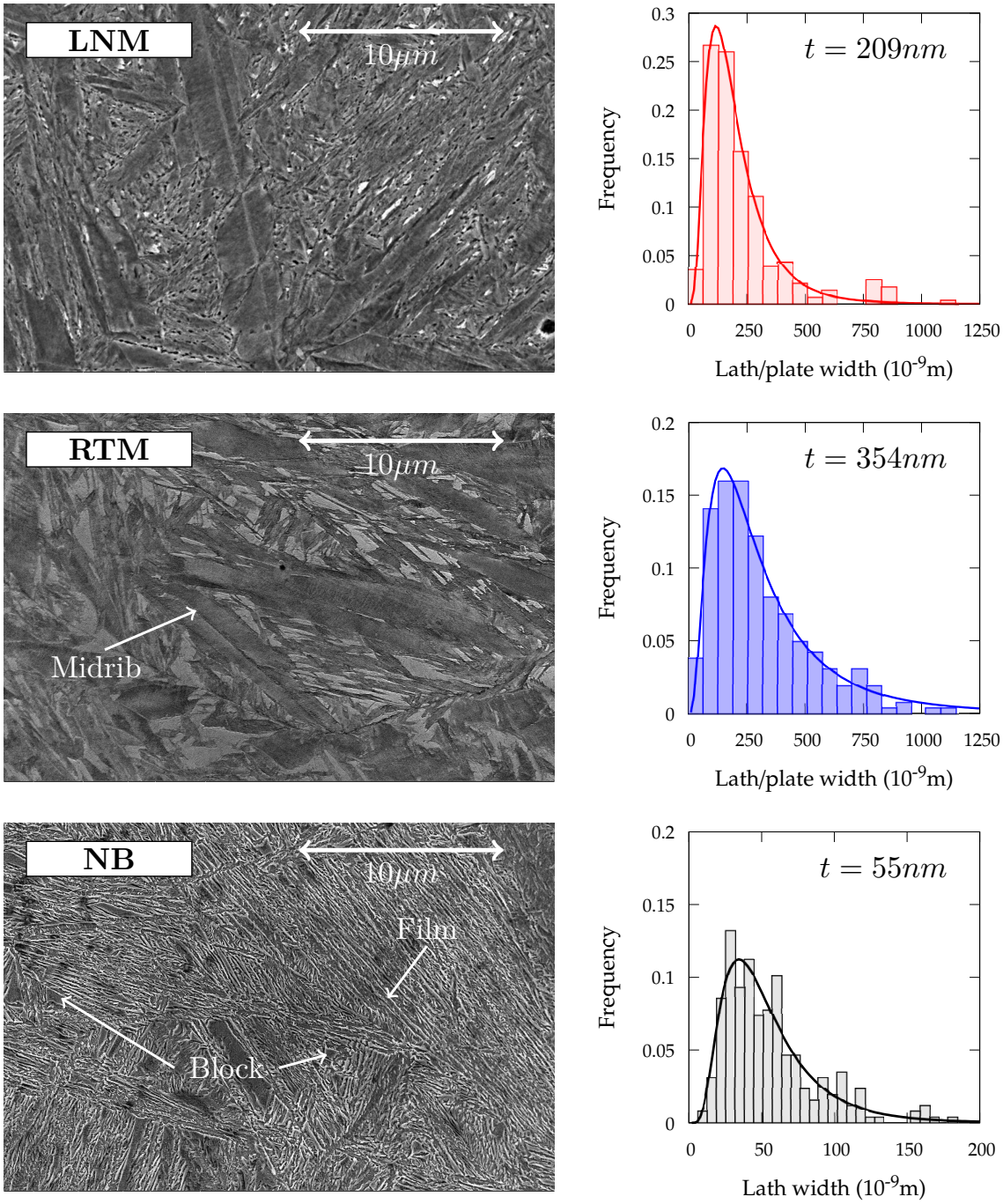

Figure 1: Scanning secondary electron microscopy micrographs for the three microstructures; plate-lath sizes distributions along with log-normal fits.

The measured hardnesses are respectively 875±10, 799±10 and 605±12 Hv-30 for LNM, RTM and NB microstructures. As expected, hardness is higher for LNM than RTM due to the higher fraction of martensite and to the smaller plates-laths sizes. Hardness of NB microstructure is much lower due to the higher fraction of retained austenite and to lower carbon content in solid solution in the bainitic ferrite (as will be seen later on) despite the finer lath size.

3.2 In situ tracking of microstructural evolutions

3.2.1 Phase fractions

Both martensite (RTM) and nanobainite formations kinetics were investigated by dilatometry and HEXRD after austenitizing at 1150°C during 3 minutes (Figure 2 and 3). Figure 2 shows the applied thermal schedules. For the NB transformation, the austempering temperature is reached rapidly (inset in b). Some examples of HEXRD diagrams are shown 2c and d at different times represented by the color code. As the transformations progresses, the austenite decomposes in martensite or in bainitic ferrite. For the NB microstructure, transition carbides (TCs) are detected after 2 hours (see the corresponding diffraction peaks in the inset).

Figure 3a and b show the deformation recorded by dilatometry and Figure 3c and d the phase fractions evolution from HEXRD, as a function of temperature for martensite and as a function of time for nanobainite (note that results are not shown above 1050°C for martensite for clarity). During the cooling, a dilatation is observed at ca. 173°C, indicating the martensite transformation start, Ms. The martensite phase fraction then increases below the Ms temperature. The averaged Ms temperature for a large number of martensitic transformations followed by dilatometry is 173±3°C considering the offset method proposed by [46] and is similar with the Ms observed by HEXRD during in situ experiment (172°C considering 1 wt.% of phase transformed), shown in Figure 3c. A good agreement is found between the measured Ms temperature and the ones calculated from empirical equations, 185°C [47] and 179°C [48]. Note that only the latter takes account of the vanadium concentration. At room temperature, the retained austenite phase fraction is 21 wt.% and no carbides due to martensite self-tempering were detected by HEXRD. The fraction of retained austenite in LNM microstructure was measured ex situ (after reheating at room temperature) and is equal to 7 wt.%.

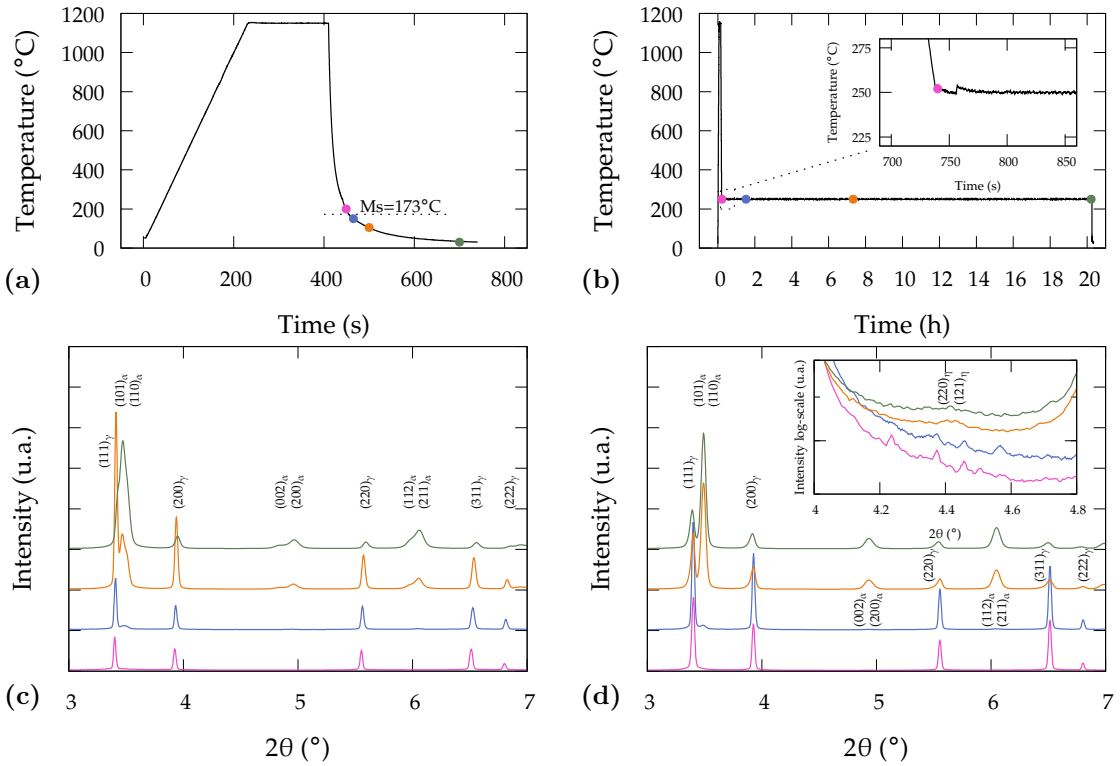

Figure 2: Thermal schedule of the **(a)** RTM and **(b)** NB transformations and associated HEXRD diagrams at different transformation times for **(c)** RTM and **(d)** NB. The inset in b) presents the transition between the cooling from the austenitization temperature to the austempering while the inset in **(d)** shows an enlarged window of the HEXRD diagrams focused on the TCs. The I/2θ diagrams presented are labeled by the colored points on the thermal schedules. Small peaks observed for nanobainite transformation time below 2 hours (inset b) are due to the presence of some large spots on the Debye-Scherrer rings after austenitization (due to the grain size) and do not correspond to any phase. The largest spots were suppressed before the circular integration.

Figures 3b and d show the nanobainite transformation kinetics (250°C during 20 h) recorded by dilatometry

and HEXRD. Time 0 corresponds to the beginning of the isothermal treatments. During the cooling from 1150°C, no transformation was observed, neither by dilatometry nor by HEXRD experiments (Figure 2d). As expected, a length increase is observed during the isothermal holding, which is related to the bainite transformation (Figure 3b). After 8 hours, the transformation kinetics slows down but continues at a slower rate until the end of the treatment, letting assume that the transformation is perhaps not complete. No phase transformation was observed by dilatometry during the cooling following the bainite transformation. This was confirmed by HEXRD.

Figure 3d shows the phase fractions evolutions obtained from HEXRD. The ferrite fraction evolution is in good agreement with the dilatometry. While the bainite transformation progresses, two phenomena occur: the enrichment in carbon of the austenite and the precipitation of TCs. The austenite also becomes heterogeneous in carbon composition, which eventually gives an asymmetric shape to the corresponding diffraction peaks. The austenite peaks analysis was performed with two austenites (carbon-rich and poor austenites with respectively higher and lower mean lattice parameters) during the Rietveld analysis, as done in [3]. It is known [3,49] that rich and poor austenites correspond to the austenite morphologies mentioned above, respectively in films between bainite laths and in blocks between bainite sheaves. Such heterogeneities were also observed in quenching and partitioning steels [50].

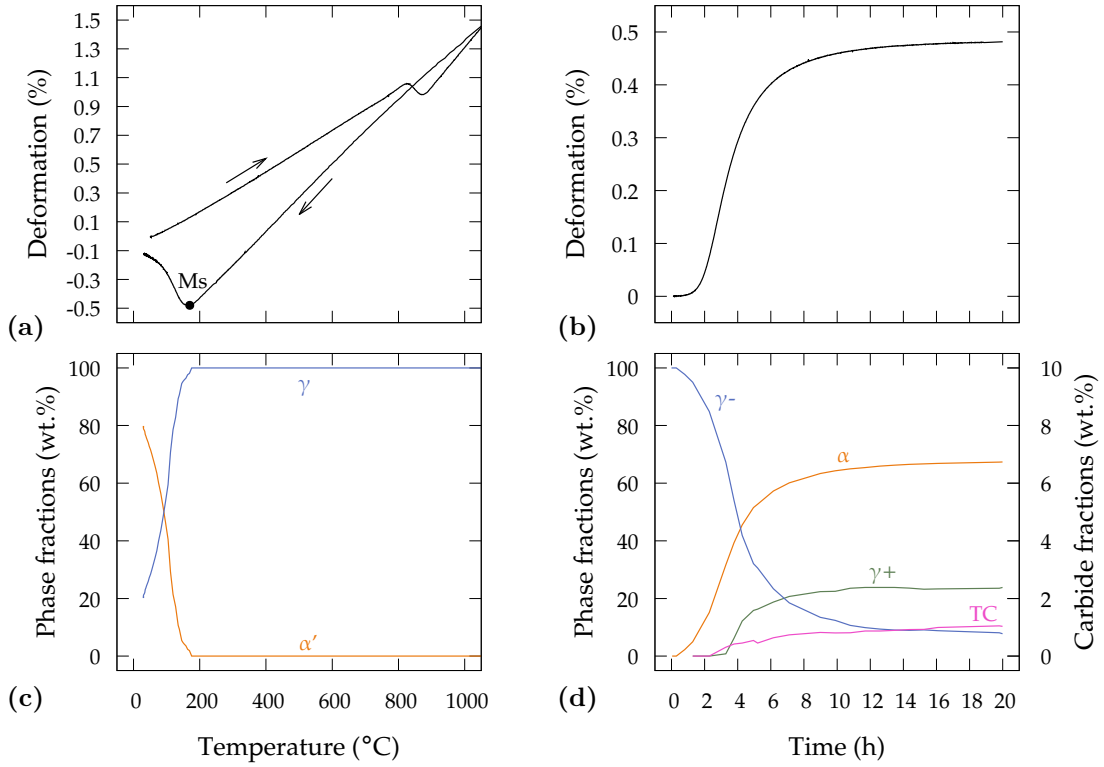

Figure 3: Phase transformation kinetics from dilatometry experiments (**(a)** and **(b)**), phase fractions evolutions from HEXRD (**(c)** and **(d)**) for martensite and nanobainite transformation respectively as function of temperature or time.

Until 4 hours, no peaks asymmetry is observed, after which the peaks start to show a skewness towards lower angles. Figure 4 shows an example of austenite peaks at the end of austempering of NB transformation and its mean Rietveld refinement. Austenite peaks show a skewness toward lower angles that cannot be associated only with micro strains and crystallite size effects. The increase of the carbon-rich austenite fraction is well correlated with the one of ferrite, apart from an initial time shift of ca. 2 h, which can be ascribed to the difficulty to deconvolute the austenite peaks.

The precipitation of TCs is quantified very early in the nanobainite transformation i.e. after 2 h which represent ca. 20 wt.% of bainitic ferrite formed. Probably these carbides were present before 2 h, but below the detection limits (size, mass fraction). The presence of TCs was also reported in [49,51], but at the end of the nanobainite transformation. In [3], η carbides were detected and quantified ex situ from HEXRD and TEM investigations, after nanobainite transformation in conditions close to present study. Carbides were actually

also detected at early stage during an in situ experiment, according to the XRD diagrams presented in [3]. Cementite was also detected in [3], but this was not the case in our study.

Hence, at the end of the nanobainite transformation, four phases are present: bainitic ferrite, two austenites (carbon-rich and poor) and transition-carbides. Our results show that the nanobainite already reaches an advanced stage of tempering at the early stages of the austempering. This is not the case for the martensite, which shows no detectable precipitation of carbides (i.e. there is no evidence of auto-tempering). The phase fractions of each constituent measured by HEXRD at room temperature (as-transformed) are summarized in Table 2.

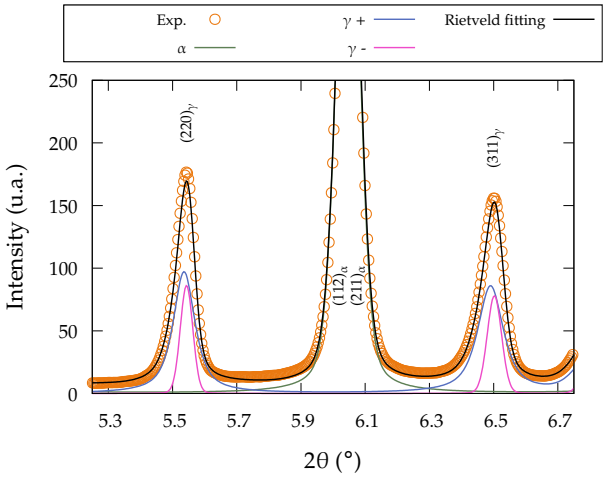

Figure 4: Reduced window of experimental HEXRD diffractogram for NB microstructure at the end of the austempering at 250°C and the associated mean Rietveld refinement. Experimental: circle; mean Rietveld refinement: black line; bainitic ferrite (α): green line; carbon rich austenite ($\gamma+$): blue curve and carbon poor austenite ($\gamma-$): pink curve.

Table 2: Phase fractions in weight in the investigated microstructures after transformation, measured from HEXRD at room temperature. The typical absolute error is ±1%, but a larger error can be expected for the TCs, due to the low peak intensities.

Microstructure	$f^{\alpha'/\alpha}$	$f^{\gamma/\gamma+}$	$f^{\gamma-}$	f^{TC}
LNM	0.93	0.07	-	-
RTM	0.79	0.21	-	-
NB	0.67	0.21	0.11	0.01

3.2.2 Lattice parameters

Thanks to the Rietveld analysis, the mean lattice parameters of investigated phases are recorded during the transformation. Generally, their evolutions during phase transformations are related to the temperature, the internal stresses and the chemical composition variations [50, 52, 53].

The lattice parameter evolutions of martensite/bainitic ferrite and austenite are shown respectively in Figure 5 and 6. The c/a ratio is also plotted in Figure 5. At the very beginning of the martensitic transformation (Figure 5a), the c and a parameters of the martensite respectively increase and decrease sharply in a first stage. These variations at the beginning of the transformation are actually ascribed to the low precision related to the low fraction of martensite. Then, both c and a parameters decrease during cooling and c/a ratio increases. These evolutions could be due to the internal stresses generated in martensite as it forms. These stress states result from the accommodation of the deformation associated with martensitic transformation (shear and volumic variation). These stress states are complex (let us mention also high elastic anisotropy in martensite [54]) and their knowledge would need further investigations (experimentally and by micromechanics). Cell parameter evolutions could also be due to carbon redistribution within the martesnite phase of heterogeneities inherited from austenite. The c/a ratio measured at room temperature is 1.0231 for RTM and 1.0212 for LNM. The solid solution carbon concentration within martensite are 0.47 wt.% for LNM and 0.51 wt.% for RTM using

the proportionality constant between the tetragonal ratio and the carbon in solid solution $k_C^\alpha = 0.045$/wt.% from [20].

Before the martensitic transformation, the austenite cell parameter (Figure 6) decreases linearly down to the Ms temperature (slight temperature dependence of the thermal expansion coefficient is mentioned though in [55]). When the martensite starts to form, the mean austenite lattice parameter deviates from the pure thermal contraction. Due to the diffusion-less nature of the martensitic transformation, this decrease cannot be interpreted as a change in chemical composition; it is attributed to a mean compressive stress state. With the temperature decrease, the mean compression stress increases. Similar evolutions were already observed during martensitic transformation followed by in situ methods [52,53,56,57]. In some cases, the austenite went into tension in a first stage, but it always reached a compression state, with the progression of the martensitic transformation. This change from the mean tension to compression state is not very well understood in the literature and could be related to the loss of percolation between the austenite islands. Further analysis of the stress states in the phases (for instance micromechanics) is needed. Generally the higher the martensite phase fraction, the higher the mean compression stress in austenite. Estimate of the hydrostatic component of the stress ($\sigma_H = 3\epsilon_L K$ where σ_H is the hydrostatic stress, ϵ_L is the deformation and K the bulk modulus) gives respectively 3.9 and 2.5 GPa for LNM and RTM at room temperature (how to derive ϵ_L from a_γ is detailed in reference [39]), in agreement with the higher and lower fractions of austenite respectively. These values are higher than in [52, 56–58].

During the nanobainite transformation, both a and c lattice parameters and c/a ratio are mostly constant. The increase at the beginning is, like for martensite, attributed to a low accuracy in lattice parameters determination. As will be seen in Section 4, the final c/a ratio (1.0082 which is close to values found in literature and leads to a carbon content in solid solution of 0.18 wt.% [20]) shows that a significant part of the carbon did not remain in solid solution in the ferrite, which nevertheless remained supersaturated. This carbon either contributed to TCs precipitation or it partitioned to the austenite. The constant c/a ratio shows that both latter processes are very fast compared to the global kinetics of the nanobainite transformation. This was also observed in [3].

During the nanobainite transformation, the lattice parameters of both austenites, carbon-rich and poor, were investigated (Figure 6b). At the beginning of the transformation the slight decrease of the carbon-poor austenite mean lattice parameter is related to experimental uncertainties. Simultaneously with the bainite transformation, the lattice parameter of the carbon-poor austenite increases due to carbon partitioning from the bainitic ferrite. Conversely, the lattice parameter of the richest austenite remains constant. From the austenite lattice parameter increase during the transformation, the carbon enrichment can be calculated through a Vegard law ($\Delta w_C = \Delta a^\gamma / k_C^\gamma$) [59], neglecting the possible effect of internal stresses. Then the carbon content at the end of transformation is the sum of this enrichment and the initial concentration ($w_C^\gamma = w_C^0 + \Delta w_C$). The austenite compositions calculated by using the proportionality constant $k_C^\gamma = 0.033$ Å/wt.% (see review in [60]) are: carbon-rich 1.24 wt.%C and carbon-poor 0.79 wt.% respectively a Δa^γ of 0.0187 Å and 0.0039 Å. These values are lower than the T_0' criterion, the austenite concentration beyond which a diffusion-less austenite ferrite becomes no more possible (see [5]): 1.4 wt.%C at 250°C, assuming a stored elastic energy of 400 J/mol and using Thermocalc software and TCFE9 database. This value is close to that of the carbon-rich austenite, in agreement with the diffusion-less theory of bainite transformation. The gap may be explained in part by the fact that the bainite transformatino is not yet finished after 20 hours (Figure 4).

Finally, it should be mentioned that the retained austenite remained fully stable upon cooling from 250°C to room temperature. Fresh martensite only formed in a range from 2°C to -150°C, as shown by dilatometry and cooling in liquid nitrogen [39]. This stability does not come only from the carbon enrichment, as the Ms expected in carbon-rich and poor austenite is about 50°C and 150°C according to empirical formulas [47, 48]. It also comes from the small size of the austenite grains (both blocks and films morphologies), as elaborated in [39], where the semi-empirical model of [61] relating the Ms and the austenite grain size was applied.

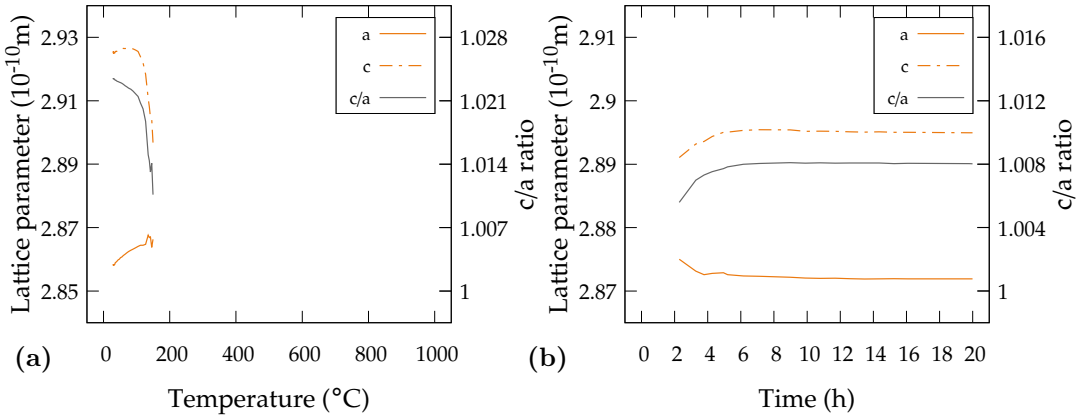

Figure 5: Martensite **(a)** and bainitic ferrite **(b)** lattice parameters and c/a ratio evolutions for both transformations as function of temperature and time respectively.

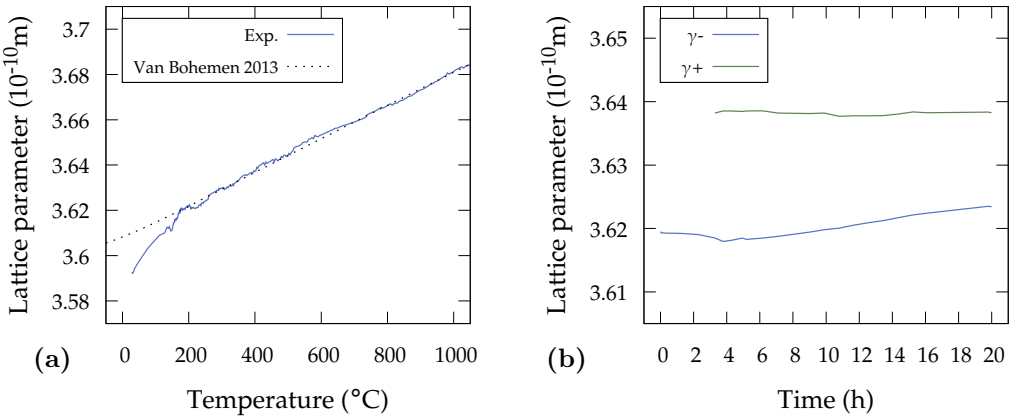

Figure 6: Martensite **(a)** and nanobainite **(b)** austenite lattice parameters evolutions for both transformations as function of temperature and time respectively.

3.2.3 Dislocation densities

The modified Williamson-Hall method was used to determine in situ by HEXRD the evolution of the dislocation density during the martensitic transformation and during the nanobainite transformation. Figure 7 shows the dislocation densities within the martensite and bainitic ferrite phases as a function of the martensite/bainitic ferrite fraction.

During the martensitic transformation, the dislocation density increases in the RTM sample. It is nearly proportional to the martensite fraction and extrapolation to higher martensite phase fraction is in good agreement with the dislocation density at room temperature which was measured ex situ for the LNM sample. These measurements give an average value ($\bar{\rho}$), but the dislocation density is actually heterogeneous in the microstructure. As described in [12], one can derive from the evolution of $\bar{\rho}$ the dislocation density specific to the new forming plates of martensite, denoted ρ^*. For example, the first formed martensite has a dislocation density of ca. $2{\times}10^{15}/\mathrm{m}^2$ while the last one (100% of martensite) has ca. $11{\times}10^{15}/\mathrm{m}^2$. This increase of ρ^* can be explained in part by the matrix work-hardening during the martensitic transformation. The first martensite plate is formed in a soft austenite matrix; it work-hardens the surrounding austenite because of the lattice invariant deformation and of the volume expansion. Then the following martensite plates form in a work-hardened austenitic matrix with higher dislocation density, but also higher resistance to plastic deformation, because of the decreasing temperature [12]. Let us mention that in our approach, broadening of diffraction peaks is only related to dislocation densities and does not take into account possible internal stress heterogeneities as martensitic transformation proceeds. Such heterogeneities were observed after transformation in [62]. The increase of the dislocation density was also reported in literature by in situ neutron diffraction analyses on stainless

steel [11] and HEXRD on a low-alloyed steel [12]. In latter study, ρ^* evolved in a lower range $2{\times}10^{14}/\mathrm{m}^2$ to $2{\times}10^{15}/\mathrm{m}^2$. This is ascribed to the lower carbon content of the investigated steel, 0.215 wt.%C, instead of 0.67 wt.%C in present study, giving lower phase transformation strains. As reported in literature [25], higher carbon concentration is correlated with higher dislocation density in martensite. Due to the higher Ms in [12], the martensitic transformation also occurred in a softer austenite.

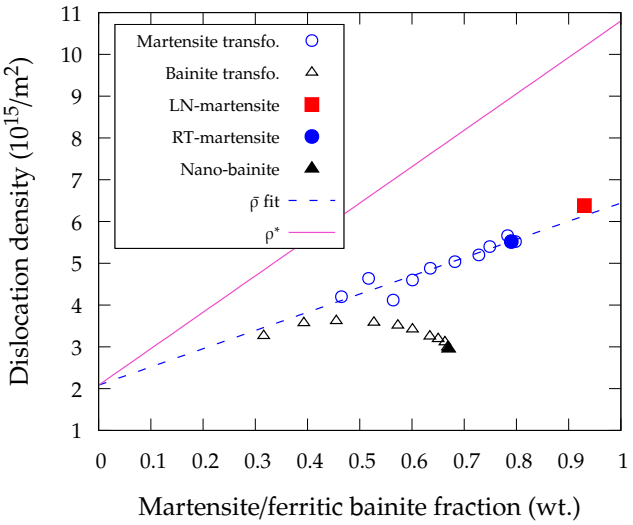

Figure 7: Dislocation densities within martensite and bainitic ferrite as a function of martensite/bainitic ferrite fraction transformed. Open circles: dislocation densities measured during martensitic and bainite transformation; dashed line: linear fit; filled symbols: dislocation densities at room temperature for the three initial microstructures; continuous red line is the calculated dislocation density of the new forming martensite plates ρ^*.

During the nanobainite transformation, the dislocation density increases in a first stage before decreasing. During the increase, the average dislocation density $\bar{\rho}$ seems to follow the same linear trend as for the martensite up to ca. 45 wt.% Hence, the evolution of the dislocation density is similar for nanobainite and martensitic transformations, despite the difference in transformation temperatures. (The martensitic transformation starts at 173°C and the austempering temperature is 250°C). Actually, this difference in transformation temperatures is not expected to lead to very large differences in dislocations densities according to the literature. For example, according to [5] (Figure 2.11), the upper bound of dislocation density measured at room temperature for a martensitic transformation starting at 173°C and austempering at 250°C are very close, respectively $7{\times}10^{15}/\mathrm{m}^2$ and $6{\times}10^{15}/\mathrm{m}^2$.

The similar dislocation densities in both microstructures may also be related to the phase transformation strains which are close for martensitic and bainite transformations [5], athough the bainite transformation occurs at higher temperature than the martensitic transformation and thus in a softer austenite.

According to the results reported in literature at room temperature and dislocation recovery observed during the austempering (see below), it is not surprising, in this case, to observe a similar dislocation density at the beginning of the two transformations. The increase of the dislocation density with the progression of the bainite transformation is also in agreement with TEM observations reported in [6–8]. The phase transformation strains would induce plastic deformation of the austenite. The resulting dislocations would be inherited by the forming ferrite laths. Reference [7] also reports heterogenous dislocation densities among different laths and inside each particular lath. This is also in agreement with our experiments, because the increase of $\bar{\rho}$ shows that the instantaneous dislocation density ρ^* increases with the progression of the phase transformation. Let us mention that for our experiments, the Williamson-Hall method could not be used to determine the dislocation density in austenite, because the carbon concentration was heterogeneous in this phase, which made impossible to analyze the broadening of the diffraction peaks.

The final decrease of $\bar{\rho}$ is ascribed to recovery. As shown in Figure 8, the first 45 wt.% of bainitic ferrite are formed in less than 4 hours, while the rest is formed in 16 hours. Hence, the recovery has a weaker impact on the first stage of the curve, which explains the increase of $\bar{\rho}$. In order to examine further the impact of the dislocations recovery, the model of Friedel et al. (see [63]) is applied here. The rate of dislocations recovery is

calculated as follows:

$$\frac{d\rho}{dt} = -K \exp\left(\frac{-U_0/N_a + VM\alpha\mu b\sqrt{\rho}}{k_B T}\right)\frac{2\sqrt{\rho}}{M\alpha\mu b} \tag{3}$$

where α was set to 0.15, N_a is the Avogadro number, k_B the Boltzmann's constant, M the Taylor factor set to 3, μ the shear modulus, as given in [64], b the Burgers vector modulus equal to 2.55 Å, and T the temperature. The activation energy U_0 was set to 251 kJ/mol (iron self-diffusion), V to $19b^3$ and K to 45×10^{15} Pa/s, as discussed in [39]. The latter values were adjusted on the basis of recovery kinetics established during tempering of RTM microstructures at 450, 550 and 650°C.

Depending on its time of formation, each bainitic ferrite lath undergoes a specific time of recovery. The model is applied to estimate the average dislocation density in the microstructure ($\bar{\rho}$). For simplicity, it is assumed that each newly formed bainitic ferrite lath has the same dislocation density ρ^* as a function of the phase fraction as was estimated for the martensite (Figure 8). This is suggested by the fact that the average dislocation density in bainite nearly follows the one of martensite in a first stage, when no significant recovery has occurred. Figure 8c shows the simulated evolution of $\bar{\rho}$. It reproduces well the experimental trend, with an increase followed by a decrease. However, the decrease of $\bar{\rho}$ starts too early; this is ascribed to the recovery model parameters which were set on the basis of experiments at higher temperatures. Almost perfect match can be achieved but by setting the K parameter of equation 3 to 2×10^{16} Pa/s and the V parameter to 20 b^3. Figure 8c shows also the important contribution of recovery through the simulation without recovery.

Let us mention that the dislocation densities found by in situ HEXRD method are close to values of literature reported for martensite and nanobainite. From measurements by TEM, [25, 27] report a dislocation density of $5\times10^{15}/\mathrm{m}^2$, for martensite in steels with 0.7 wt.%C. For nanobainte formed at 300°C during three days, [7] reports a value of $0.5\times10^{15}/\mathrm{m}^2$. In the case of nanobainite, values obtained by XRD are 3.5 and $3.1\times10^{15}/\mathrm{m}^2$ respectively for nanobainite formed at 220°C for 22 h and 250°C for 16 h [3] and $4.8\times10^{15}/\mathrm{m}^2$ for 2 h at 390°C [30]. Hence, the dislocation densities measured by TEM tend to be lower than those estimated by XRD [26, 27]. This can be due to dislocation density heterogeneities that are not captured by TEM but also to an over-estimation of the dislocation density by XRD.

One can also mention that the martensitic microstructures have more heterogeneous dislocation densities than the nanobainite, which underwent recovery. This has an impact on the mechanical behavior [12, 65]. This heterogeneity comes in addition to the more scattered sizes reported in Section 3.1.

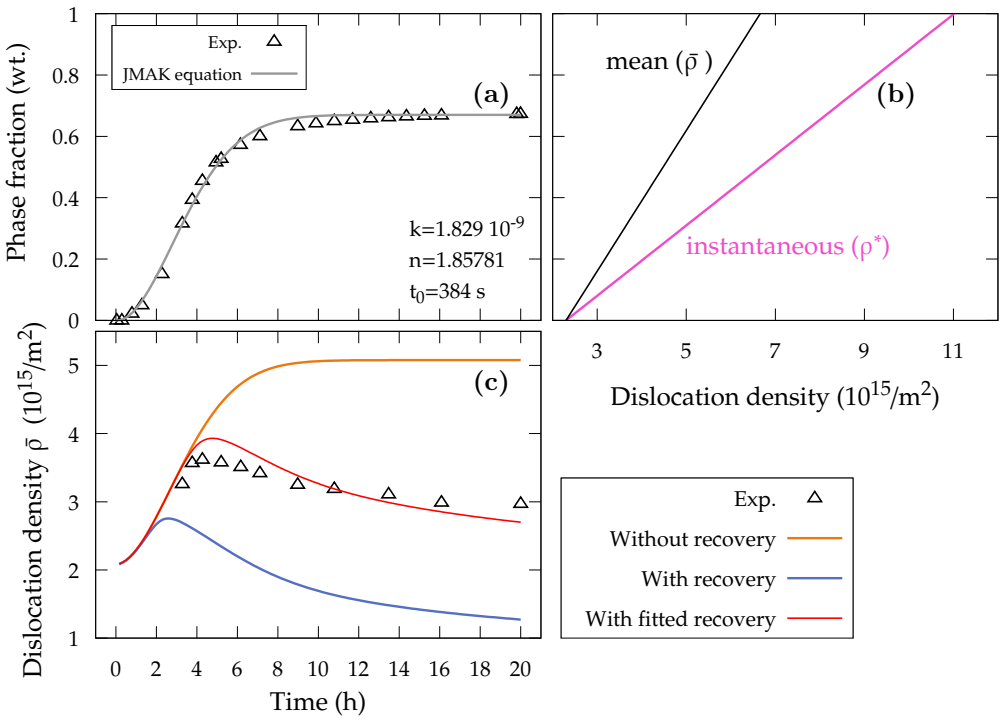

Figure 8: **(a)** Bainitic ferrite fraction vs. time with JMAK fitting, **(b)** estimated instantaneous dislocation density ρ^* in new forming bainitic laths and **(c)** measured average dislocation density in the microstructure ($\bar{\rho}$) according to the experiment and to the simulation of average dislocation density with different assumptions (see in the text).

4 Carbon distribution inside the microstructures

4.1 Carbon mass balance

It is of interest to determine how the carbon is distributed between the austenite, the bainitic ferrite or the martensite. Inside both latter phases, the carbon can be segregated to defects (dislocations, planar boundaries), gathered in clusters or iron carbides, while the remaining part is in solid solution. From the HEXRD results presented before regarding phase fractions, lattice parameters and dislocation densities, could we determine how the carbon is distributed in the final microstructures?

The amount of carbon in solid solution in austenite, in martensite or in bainitic ferrite is equal to:

$$f^{\phi} w_C^{\phi} \tag{4}$$

where f^{ϕ} is the mass fraction of phase ϕ and w_C^{ϕ} is the carbon mass concentration in solid solution in phase ϕ, either bainitic ferrite/martensite (α), austenite (γ) or, in nanobainite, rich and poor austenite ($\gamma+$ and $\gamma-$).

Determinations of phase fractions were presented in Section 3.2.1. The carbon concentration in solid solution in martensite or bainitic ferrite is related to the c/a ratio of the quadratic cell, through the equation 5.

$$c/a = 1 + k_C w_C(wt.\%) \tag{5}$$

where k_C is an experimental constant, and w_C the carbon concentration in solid solution.

The proportionality constant $k_C = 0.045$/wt.% from reference [20] is used. Estimations of the carbon concentration in solid solution in austenite were presented in Section 3.2.2. In nanobainite, the transition iron carbides (TCs) have to be considered in addition. the amount of carbon in the transition carbides is equal to $f^{TC} w_C^{TC}$. A composition of 8.4 wt.% C (30 at.% - $Fe_{2.4}C$) is assumed inside the TCs. In the austenite, the amount of carbon segregated to defects is assumed to be negligible, because of the lower dislocation density [11,12], and also of the slower carbon diffusion. Conversely, carbon segregation to defects has to be considered

in martensite and nanobainitic ferrite. The former undergoes autotempering and for the latter, the duration of the treatment gives enough time for segregation to occur, in addition to TCs precipitation [3,19,66,67].

We followed the same approach as in [3,19] to estimate the amount of carbon segregated to defects. Three contributions are considered:

- density change due to dislocations,
- Cottrell atmospheres along dislocations,
- ferrite/austenite interfaces or martensite lath boundaries.

In the following, only the segregation to dislocations will be considered, whereas the segregation to planar defects will by considered separately in Section 4.2. The first contribution refers to the regions of the lattice which are expanded due to the stress field of the dislocations. Some carbon can occupy these regions without distorting the lattice, and the corresponding number of carbon atoms per unit volume of ferrite is denoted N_v^C. The respective volume changes induced by the strain field of the dislocations and by the carbon atoms should be equal [3,19], leading to :

$$N_v^C = \rho \frac{\Gamma ln(R/r_0)\Omega}{b\Delta V_C} \tag{6}$$

where $\Gamma ln(R/r_0)$ is the volume change per atomic volume Ω due to a dislocation with a length equal to the Burgers vector b, R and r_0 are respectively the dislocation outer and core radius, and ΔV_C is the volume change due to the insertion of a single carbon atom into a unit cell of bcc iron, and ρ the dislocation density. The parameters used are $\Gamma = 0.34$ corresponding to a mixture of 50% screw and 50% edge type dislocations [68], R = 60 nm, r_0 = 1.25 nm, b = 0.25 nm, $\Omega = 4b^3/3^{3/2}$ nm^3, and $\Delta V_C = 7.8{\times}10^{-3}$nm^3. Then the atomic percent concentration of carbon which can be inserted without altering the lattice parameter is given by:

$$C_\alpha^\rho = 100 N_v^C \Omega \tag{7}$$

The atomic percent concentration of carbon trapped by Cottrell atmospheres (the second contribution) was calculated by considering that dislocations with Cottrell atmospheres can trap ca. 8 at.% (1.83 wt.%) of carbon and that the carbon is segregated inside a cylinder of radius r_0 = 1.25 nm. Thus the Cottrell atmospheres are described as cylinders of radius r_0 with a length equal to the dislocation density filled with 8. at.% of carbon:

$$C_\alpha^{Cottrell} = 8\rho\pi r_0^2 \tag{8}$$

The total mass fraction of carbon segregated to dislocations ($w_C^{\alpha,\ defects}$) is the sum (after conversion from atomic to mass fractions) of both previous contributions (C_α^ρ and $C_\alpha^{Cottrell}$).

Table 3 shows the amount of carbon segregated to the dislocations in the three initial microstructures (in weight percent). It appears that up to about 10% of the carbon content of the steel (0.67 wt.%) may segregate to dislocations. The amount segregated is two times higher in LNM than in NB microstructure, as expected from the higher dislocation density. A large part of the carbon segregated is trapped by Cottrell atmospheres (ca. 80%), whereas the contribution related to the volume changes is weak, and probably in the experimental error. The values calculated are in good agreement with the literature [3,19,69,70] [1].

Table 3: Estimation of the carbon amount segregated with contributions from the volume change ($w_C^{\alpha,\ \rho}$), the Cottrell atmospheres ($w_C^{\alpha,\ Cotrell}$). $w_C^{\alpha,\ defects}$ is the sum.

Microstructure	$\bar{\rho}^\alpha$ (10^{15}/m^2)	$w_C^{\alpha,\ \rho}$ (wt.%)	$w_C^{\alpha,\ Cotrell}$ (wt.%)	$w_C^{\alpha,\ defects}$ (wt.%)
LNM	6.4	0.013	0.057	0.070
RTM	5.6	0.012	0.050	0.062
NB	3.0	0.006	0.027	0.033

Table 4 shows the phase fractions (f^ϕ) and the carbon distribution among the phases and the defects. $w_C^{\alpha,\ defects}$ is scaled by the fraction of bainitic ferrite or martensite. Figure 9 shows graphically these results.

[1] Note that in [3] the authors omitted the Γ parameter in equation 6 and that in [19] the r_0 parameter is note clearly well defined.

The percentages are calculated for each contribution with respect to the overall carbon composition of the steel (0.67 wt.%). In both martensite microstructures, a large part of the carbon is in solid solution within the martensite, while the austenite kept the nominal composition of the steel. Due to a higher dislocation density, more carbon is trapped at defects in LNM than in RTM. The carbon distribution in NB is very different: retained austenite contains about one half of the carbon, due to the partitioning during the austempering. Contrary to both martensites, carbides are present and, despite a low fraction (1 wt.%), these carbides contain a large amount of the carbon. Clearly, it is more difficult to achieve the mass balance in presence of the TCs, because of the uncertainty on their mass fraction and their stoichiometry; the amount of carbon trapped by the carbides may be higher.

Table 4: Phase fractions (wt.%) and carbon content distribution (wt.%) in martensites and nanobainite microstructures.

	f^{α}	$f^{\gamma+}$	$f^{\gamma-}$	f^{TC}	$f^{\alpha}w_C^{\alpha}$	$f^{\gamma+}w_C^{\gamma+}$	$f^{\gamma-}w_C^{\gamma-}$	$f^{TC}w_C^{TC}$	$f^{\alpha}w_C^{\alpha,\ defects}$	$w_C^{deficit}$
LNM	0.93	0.07	-	-	0.437	0.047	-	-	0.065	0.121
RTM	0.79	0.21	-	-	0.403	0.141	-	-	0.049	0.077
NB	0.67	0.21	0.11	0.01	0.121	0.260	0.086	0.084	0.022	0.097

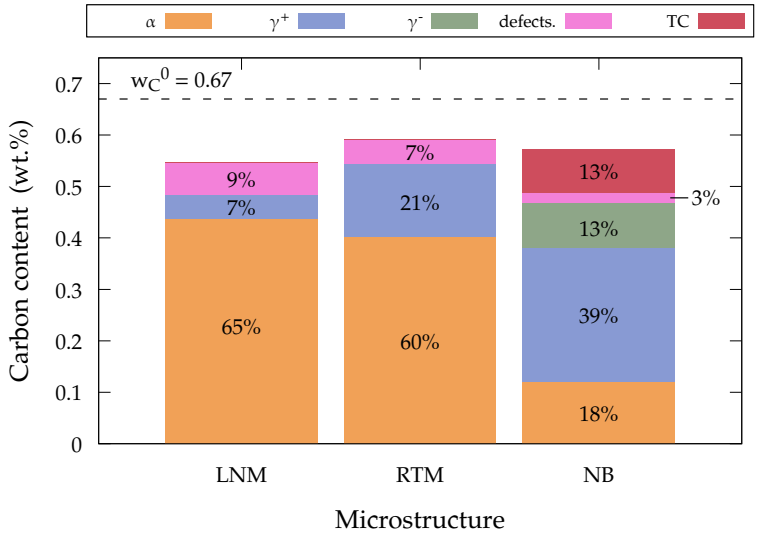

Figure 9: Carbon content distribution within martensites and nanobainite initial microstructures.

4.2 Origins of the carbon deficit

The carbon deficit is defined as the carbon content of the steel ($w_C^0 = 0.67$ wt.%) minus all the contributions ($w_C^0 - \Sigma f^{\phi} w_C^{\phi}$). The carbon deficit is equal to ca. 0.1 wt.% (from 0.077 to 0.121 wt.%) for the three initial microstructures, which represents ca. 15% of the overall carbon content. Similar discrepancies were found in previous studies, [3,4,6,18], and three possible origins are now considered.

First possible origin regards the carbon in solid solution in the martensite or the bainitic ferrite phases, which is estimated from the c/a ratio through the equation 5. This relationship is actually not yet firmly established. Two values of the proportionality constant have been proposed in literature ($k_C = 0.031$ or 0.045/wt.%) [20,21]. The alloying elements also influence the c/a ratio [71,72] and the relationship could even be non-linear [22,73]. Another issue regards the accounting or not of the carbon segregated to defects in this relationship. According to some studies combining XRD and APT (e.g. [13]), this carbon does not make increase the overall c/a ratio. It should thus be counted separately in the mass balance, like we did in Figure 9. Other studies suggest that one part of the carbon out from the solid solution also makes increase the c/a ratio. This is the case for instance in [74], which have shown that carbon in clusters (but not segregated) inside nanobainitic ferrite may increase the c/a ratio. These uncertainties on the link between the c/a ratio and the carbon concentration in solid solution may explain our carbon deficit: the carbon concentration inside the bainitic ferrite or the martensite would be underestimated. To verify this, we back-calculated the carbon concentrations which should be found in the bainitic ferrite or the martensite to achieve the carbon mass balance. The results are presented in Table

5 with two assumptions: either a part of carbon is segregated to defects (i.e. this part does not contribute to the solid solution, column $w_C^{\alpha}(\gamma,\ TC, defects)$) or not (i.e. this part contribute to the solid solution, column $w_C^{\alpha}(\gamma,\ TC)$). Then, the coefficient k_C of equation 5 linking the carbon concentration and the tetragonality, is re-calculated.

For both martensites, the coefficients k_C are close to the one reported by [21], ($k_C = 0.031$/wt.%), if it is neglected that carbon can segregate along defects. With the opposite assumption, the values of k_C remain between the boundaries given by [20] and [21] as illustrated in Figure 10. Regarding nanobainite, unexpected low values of k_C are found. But as mentioned before, the presence of the TCs strongly influences the mass balance, while their mass fraction and stoichiometry are not known with precision

Table 5: Experimental tetragonal ratio and calculated carbon content within the martensite/ferritc bainite to achieve the carbon mass balance considering the presence or not of carbon trapped on the defects.

	c/a ratio	$w_C^{\alpha}(\gamma,\ TC)$	$k_C^{\alpha}(\gamma,\ TC)$	$w_C^{\alpha}(\gamma,\ TC,\ defects)$	$k_C^{\alpha}(\gamma,\ TC,\ defects)$
LNM	1.0212	0.67	0.032	0.60	0.035
RTM	1.0231	0.67	0.035	0.61	0.038
NB	1.0082	0.36	0.023	0.33	0.025

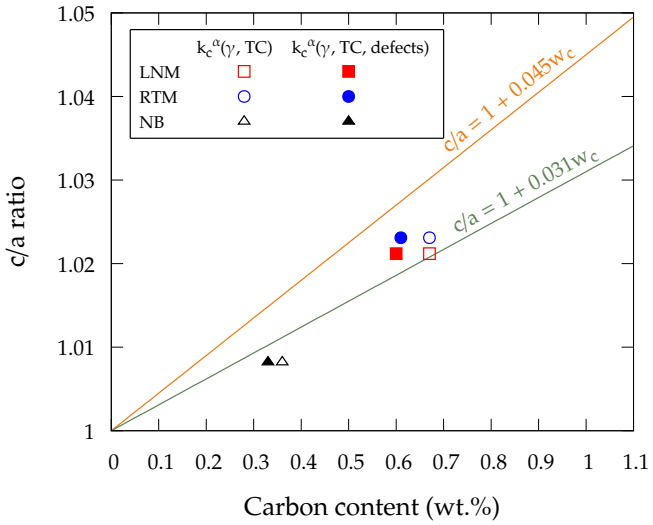

Figure 10: Comparison between the tetragonal ratio of the martensite/bainitic ferrite phase as function of carbon content considering that the carbon missing is in solid solution. Empty / full symbols: the carbon segregated at dislocations contributes / does not contribute to the increase of the c/a ratio.

The results regarding the martensite are in good agreement with the relationship given in [21] ($k_C = 0.031$/wt.%), especially if it is neglected that carbon can segregate along defects. It is thought that in [21], a large amount of carbon actually segregated to defects. Indeed, the martensite probably underwent autotempering, like in present study. This is expected from the experimental conditions reported in [21] (quench rate, sample size). Except when very fast quenching is achieved [75], autotempering occurs, as shown by TEM, APT, XRD in [13]. (In latter study, cooling rates from 500 to 2000°C/s were applied to thin samples). Hence, the values of k_C found in present study and [21] are probably underestimated because the carbon segregated to defects was not excluded from the solid solution. Conversely, when we excluded the segregated carbon, we found k_C values closer to the more conventional one ($k_C = 0.045$/wt.%), as shown in Figure 10 (filled symbols). Let us mention that in [13], a good correlation with $k_C^{\alpha} = 0.045$/wt.% was found by measuring by APT the carbon concentration in solid solution and far from defects or carbides[2]. To conclude, the conventional value $k_C^{\alpha} = 0.045$/wt.% can be considered as representative of the link between the tetragonal ratio and the carbon content truly in solid solution, whereas the value $k_C^{\alpha} = 0.031$/wt.% may be used as an estimate if the segregation of some carbon to defects is neglected.

[2]However, the XRD analysis may by questioned due to the reflection of the K_{α} 1 and 2 of the Co radiation source and the utilization of texture parameters during the Rietveld analysis, which are not clearly specified for all considered steel compositions.

Second possible origin of the carbon deficit regards the segregation to dislocations. Main parameters to estimate the amount of carbon trapped in Cottrell atmospheres are the dislocation density, the dislocation core radius (r_0 in equation 8) and the carbon concentration near the dislocation. We have a good confidence about the dislocations densities shown in Section 3.2.3. But the dislocation outer cut-off radius is not well known and large scatter of values can be found in literature. As we did for the tetragonal ratio, we back-calculated the cut-off radius by inverse calculation, such that the carbon mass balance is achieved. (Considering again $k_C^{\alpha} = 0.045$/wt.% for carbon in solid solution within tetragonal phase). In this calculation, we only consider the Cottrell contribution, while the contribution related to lattice volume expansion (equation 7) is neglected. The dislocation cut-off radii calculated for each initial microstructure are 2.4 nm for LNM, 2.3 nm for RTM and 3.3 nm for NB. The values found for both martensites are closer to the values reported in literature from modeling and APT experiments, from ca. 2 to 7 nm [76–78], than the value used initially (1.25 nm), taken from [3]. For nanobainite, the cutoff radius found is 3.3 nm, which would mean that more carbon is trapped along the dislocations than in martensites. But as mentioned for this initial microstructure, the uncertainties regarding the TCs strongly affect the mass balance.

Last origin of the carbon deficit regards carbon segregation along the plates/laths boundaries, which is mentioned in studies on martensite after quenching [75, 79, 80], martensite tempering [14, 81] and nanobainite [19,77]. Modeling was also considered in [82,83]. The surface area per unit volume of interfaces can be estimated in first approximation as:

$$S_v \sim 1/t \tag{9}$$

where t is the average plate/lath thickness which was determined from microstructural observations (Section 3.1). S_v is equal to 4.8×10^6/m for the LNM microstructure, 2.8×10^6/m for the RTM microstructure and 18.1×10^6/m for the nanobainite.

The amount of carbon segregated to planar defects is estimated as:

$$w_C^{seg.\ at\ boundaries} = S_v\ th\ w_C^{boundaries} \tag{10}$$

where $w_C^{boundaries}$ is the local carbon concentration in the segregated zone near the boundary and th is the thickness of this zone. $w_C^{boundaries}$ is about 4-5 at% [19, 80] (0.9-1.1 wt%). th is estimated to 1 nm [19]. By considering a local carbon concentration $w_C^{boundaries}$ of 1.1 wt% in the segregated zone, this gives an amount of carbon segregated to planar defects $w_C^{seg.\ at\ boundaries}$ of 5.3×10^{-3} wt% for the LNM microstructure, 3.1×10^{-3} wt% for the RTM microstructure and 19.9×10^{-3} wt% for the nanobainite microstructure. These values are far below the carbon deficit reported above, of about 0.1 wt%, even for the nanobainite, which is the finest microstructure. Hence, segregation to planar defects is negligible in the investigated microstructures.

Let us mention that the carbon segregation at nanobainitic ferrite lath boundaries could actually not be put into evidence by reported APT observations [10,19,66,77]. Regarding martensite, segregation to lath boundaries is reported in several studies [14, 75, 79–81], but in some cases, this may be ascribed to the higher dislocation density near the martensite laths [14,79]. The amount segregated also depends on the Ms, or the parameters of further tempering or Q&P treatments. For instance Aoued et al. [80] showed that the carbon content segregated at the boundaries decreases during the partitioning step of a Q&P treatment.

Finally, as already mentioned, the presence of TCs in the quenched martensite cannot be ruled out, although it was not detected by HEXRD. In nanobainite, the fraction of TCs could be slightly under-estimated due to the same reasons and difficulties in the Rietveld refinement. A small error on the carbide phase fraction can strongly affect the carbon deficit measured in both martensites and nanobainite microstructures (e.g. a TCs phase fraction variation of ±0.5% leads to a carbon variation of ±0.042 wt.%).

5 Conclusions

In situ synchrotron HEXRD has been used to track simultaneously two key microstructural features which evolve during martensitic and nanobainitic transformations: the dislocation density and the distribution of the carbon. One single High-Si steel composition and austenitization condition has been considered. Dilatometry experiments and SEM observations were carried out in addition.

As reported in previous studies on martensitic transformations, the dislocation density inside newly formed plates or laths increases with the progression of the transformation. The same evolution is observed here in the case of a nanobainite transformation. The rate of increase of the dislocation density (ρ vs. ferrite or martensite fraction) is nearly the same during the nanobainite transformation and the martensitic transformation. This is ascribed to the close transformation temperatures and transformation strains associated with both phase transformations. The resulting NB microstructure undergoes recovery in a second stage, because of the long duration, 20 hours, of the austempering treatment. Recovery kinetics is well described by a model from the literature.

Performing a carbon mass balance all along nanobainite and martensitic transformations led to the following observations:

1. The carbon segregated to dislocations represents a weak proportion of the overall carbon content of the steel. (This would have been different in a steel with lower carbon content). Segregation along planar defects is negligible, due to the small surface of plate/lath boundaries per unit volume.

2. During the nanobainite transformation, a large part of the carbon partitions from ferrite to austenite, or forms transition carbides, as expected. From the in situ characterizations, it is shown here that both phenomena are concomitant with the ferrite formation.

3. In contrast, no sign of autotempering could be detected in martensite.

4. Both martensite and nanobainitic ferrite remain largely supersaturated in carbon, in agreement with literature. In present study, it is concluded from the mass balance that the proportionality constant $k_C^{\alpha} = 0.045/\text{wt.\%}$ is representative of the link between the tetragonal (c/a) ratio and the carbon concentration in solid solution.

Author contributions: Conceptualization, S.G, J.T., D.S. and S.Y.P.A; investigation, S.G. and G.G.; writing-original draft preparation, S.G.; writing-review and editing, S.G, J.T., D.S., G.G. and S.Y.P.A; supervision, J.T. and S.D.; project administration, J.T., D.S. and S.Y.P.A. All authors have read and agreed to the published version of the manuscript.

Funding: This research was funded by the STEELSECO RFCS European project under the grant number 754070 (2017).

Declaration of competing interest: The authors declare no conflict of interest. The funders had no role in the design of the study, collection, analyses and interpretation of data in the writing of the manuscript, or in the decision to publish the results.

Acknowledgments: The material was provided by T. Sourmail from Ascometal (Hagondange, France). The HEXRD experiments were conducted at DESY (PETRAIII-P07 beamline) in Hamburg under the I-20180973 EC grant. A special thanks is dedicated to the team of the P07 line. The expertise of N. Schell and A. Stark was much appreciated and widely contributed to the success of the study.

Data availability: The raw/processed data required to reproduce these findings cannot be shared at this time as the data also forms part of an ongoing study.

References

[1] Jean-Christophe Hell, Moukrane Dehmas, Sébastien Allain, Juscelino Mendes Prado, Alain Hazotte, and Jean-Philippe Chateau. Microstructure–properties relationships in carbide-free bainitic steels. ISIJ international, 51(10):1724–1732, 2011.

[2] FG Caballero, HKDH Bhadeshia, KJA Mawella, DG Jones, and P Brown. Very strong low temperature bainite. Materials science and technology, 18(3):279–284, 2002.

[3] Rosalia Rementeria, Jose A Jimenez, Sébastien YP Allain, Guillaume Geandier, Jonathan D Poplawsky, Wei Guo, Esteban Urones-Garrote, Carlos Garcia-Mateo, and Francisca G Caballero. Quantitative assessment of carbon allocation anomalies in low temperature bainite. Acta Materialia, 2017.

[4] Samy Aoued, Frédéric Danoix, Sébastien YP Allain, Steve Gaudez, Guillaume Geandier, Jean-Christophe Hell, Michel Soler, and Mohamed Gouné. Microstructure evolution and competitive reactions during quenching and partitioning of a model fe–c–mn–si alloy. Metals, 10(1):137, 2020.

[5] Harshad Kumar Dharamshi Hansraj Bhadeshia. Bainite in steels: theory and practice. Third edition. CRC Press, 2019.

[6] Francesca G Caballero, Michael K Miller, C Garcia-Mateo, and J Cornide. New experimental evidence of the diffusionless transformation nature of bainite. Journal of Alloys and Compounds, 577:S626–S630, 2013.

[7] J Cornide, Goro Miyamoto, Francisca Garcia Caballero, Tadashi Furuhara, Michael K Miller, and Carlos Garcia-Mateo. Distribution of dislocations in nanostructured bainite. In Solid State Phenomena, volume 172, pages 117–122. Trans Tech Publ, 2011.

[8] I. B. Timokhina, K. D. Liss, D. Raabe, K. Rakha, H. Beladi, X. Y. Xiong, and P. D. Hodgson. Growth of bainitic ferrite and carbon partitioning during the early stages of bainite transformation in a 2%mass silicon steel studied by *in situ* neutron diffraction, TEM and APT. Journal of Applied Crystallography, 49(2):399–414, Apr 2016.

[9] Francesca G Caballero, Michael K Miller, C Garcia-Mateo, C Capdevila, and Suresh S Babu. Redistribution of alloying elements during tempering of a nanocrystalline steel. Acta materialia, 56(2):188–199, 2008.

[10] C Garcia-Mateo, JA Jimenez, H-W Yen, Michael K Miller, L Morales-Rivas, M Kuntz, SP Ringer, J-R Yang, and Francesca G Caballero. Low temperature bainitic ferrite: Evidence of carbon super-saturation and tetragonality. Acta Materialia, 91:162–173, 2015.

[11] Frédéric Christien, MTF Telling, and KS Knight. Neutron diffraction in situ monitoring of the dislocation density during martensitic transformation in a stainless steel. Scripta Materialia, 68(7):506–509, 2013.

[12] Macchi Juan, Gaudez Steve, Geandier Guillaume, Teixeira Julien, Denis Sabine, Bonnet Frédéric, and YP Allain Sébastien. Dislocation densities in a low-carbon steel during martensite transformation determined by in situ high energy x-ray diffraction. Materials Science and Engineering: A, page 140249, 2020.

[13] Naoki Maruyama, Shinichiro Tabata, and Hiroyuki Kawata. Excess solute carbon and tetragonality in as-quenched fe-1mn-c (c: 0.07 to 0.8 mass pct) martensite. Metallurgical and Materials Transactions A, 51(3):1085–1097, 2020.

[14] Annika Vieweg, Erwin Povoden-Karadeniz, Gerald Ressel, Petri Prevedel, Tomasz Wojcik, Francisca Mendez-Martin, Andreas Stark, Jozef Keckes, and Ernst Kozeschnik. Phase evolution and carbon redistribution during continuous tempering of martensite studied with high resolution techniques. Materials & Design, 136:214–222, 2017.

[15] C Garcia-Mateo, M Peet, FG Caballero, and HKDH Bhadeshia. Tempering of hard mixture of bainitic ferrite and austenite. Materials Science and Technology, 20(7):814–818, 2004.

[16] Chih Yuan Chen, Chien Chon Chen, and Jin-Shyong Lin. Morphology feature of nanostructure bainitic steel after tempering treatment. World Academy of Science, Engineering and Technology, International Journal of Mechanical, Aerospace, Industrial, Mechatronic and Manufacturing Engineering, 8(5):928–931, 2014.

[17] G Krauss. Tempering of martensite in carbon steels. In Phase Transformations in Steels, pages 126–150. Elsevier, 2012.

[18] V Lejay, C Sidoroff, Christophe Le Bourlot, M Perez, and P Dierickx. Ageing of 100cr6 steel: synchrotron x-ray diffraction and dimensional analysis investigation. Materials Science and Technology, 32(11):1106–1110, 2016.

[19] HKDH Bhadeshia. Anomalies in carbon concentration determinations from nanostructured bainite. Materials Science and Technology, 31(7):758–763, 2015.

[20] CS Roberts. Effect of carbon on the volume fractions and lattice parameters of retained austenite and martensite. Jom, 5(2):203–204, 1953.

[21] Yuan Lu, Haixuan Yu, and Richard D Sisson Jr. The effect of carbon content on the c/a ratio of as-quenched martensite in fe-c alloys. Materials Science and Engineering: A, 700:592–597, 2017.

[22] P Maugis. Ferrite, martensite and supercritical iron: A coherent elastochemical theory of stress-induced carbon ordering in steel. Acta Materialia, 158:454–465, 2018.

[23] Francesca G Caballero, Michael K Miller, and C Garcia-Mateo. Atom probe tomography analysis of precipitation during tempering of a nanostructured bainitic steel. Metallurgical and Materials Transactions A, 42(12):3660, 2011.

[24] Hideaki Sawada, Naoki Maruyama, Shinichiro Tabata, and Kazuto Kawakami. Dependence of carbon concentration and alloying elements on the stability of iron carbides. ISIJ International, 59(6):1128–1135, 2019.

[25] S Morito, J Nishikawa, and T Maki. Dislocation density within lath martensite in Fe-C and Fe-Ni alloys. ISIJ international, 43(9):1475–1477, 2003.

[26] Shigeto Takebayashi, Tomonori Kunieda, Naoki Yoshinaga, Kohsaku Ushioda, and Shigenobu Ogata. Comparison of the dislocation density in martensitic steels evaluated by some X-ray diffraction methods. ISIJ international, 50(6):875–882, 2010.

[27] DC Saha, E Biro, AP Gerlich, and Y Zhou. Effects of tempering mode on the structural changes of martensite. Materials Science and Engineering: A, 673:467–475, 2016.

[28] GK Williamson and WH Hall. X-ray line broadening from filed aluminium and wolfram. Acta metallurgica, 1(1):22–31, 1953.

[29] T Ungár and A Borbély. The effect of dislocation contrast on x-ray line broadening: a new approach to line profile analysis. Applied Physics Letters, 69(21):3173–3175, 1996.

[30] Arijit Saha Podder. Tempering of a mixture of bainite and retained austenite. PhD thesis, Citeseer, 2011.

[31] C Garcıa De Andres, MJ Bartolomé, Carlos Capdevila, D San Martın, FG Caballero, and Víctor López. Metallographic techniques for the determination of the austenite grain size in medium-carbon microalloyed steels. Materials characterization, 46(5):389–398, 2001.

[32] Jérôme Kieffer and Dimitrios Karkoulis. Pyfai, a versatile library for azimuthal regrouping. In J. Phys. Conf. Ser, volume 425, page 36, 2013.

[33] Juan Rodriguez-Carvajal. Fullprof: a program for rietveld refinement and pattern matching analysis. In satellite meeting on powder diffraction of the XV congress of the IUCr, volume 127. Toulouse, 1990.

[34] DT Pierce, DR Coughlin, DL Williamson, KD Clarke, AJ Clarke, JG Speer, and E De Moor. Characterization of transition carbides in quench and partitioned steel microstructures by mössbauer spectroscopy and complementary techniques. Acta Materialia, 90:417–430, 2015.

[35] SW Thompson. Structural characteristics of transition-iron-carbide precipitates formed during the first stage of tempering in 4340 steel. Materials Characterization, 106:452–462, 2015.

[36] Sébastien YP Allain, Samy Aoued, Angéline Quintin-Poulon, Mohamed Gouné, Frederic Danoix, Jean-Christophe Hell, Magali Bouzat, Michel Soler, and Guillaume Geandier. In situ investigation of the iron carbide precipitation process in a fe-c-mn-si q&p steel. Materials, 11(7):1087, 2018.

[37] Arthur S Nishikawa, Goro Miyamoto, Tadashi Furuhara, André P Tschiptschin, and Hélio Goldenstein. Phase transformation mechanisms during quenching and partitioning of a ductile cast iron. Acta Materialia, 179:1–16, 2019.

[38] Setsuo Takaki, Takuro Masumura, and Toshihiro Tsuchiyama. Proposal of simplified modified williamson-hall equation. ISIJ International, 58(12):2354–2356, 2018.

[39] Steve Gaudez. Kinetics and microstructural evolutions during the tempering of martensitic and nano-bainitic low alloyed steel: In situ experimental study and modelling. Université de Lorraine, 2021.

[40] András Borbély, Juliana Dragomir-Cernatescu, Gábor Ribárik, and Tamás Ungár. Computer program anizc for the calculation of diffraction contrast factors of dislocations in elastically anisotropic cubic, hexagonal and trigonal crystals. Journal of applied crystallography, 36(1):160–162, 2003.

[41] T. Ungár, I. Dragomir, Á. Révész, and A. Borbély. The contrast factors of dislocations in cubic crystals: the dislocation model of strain anisotropy in practice. Journal of Applied Crystallography, 32(5):992–1002, Oct 1999.

[42] N Sallez, X Boulnat, A Borbély, JL Béchade, D Fabrègue, Michel Perez, Y De Carlan, L Hennet, C Mocuta, D Thiaudière, et al. In situ characterization of microstructural instabilities: Recovery, recrystallization and abnormal growth in nanoreinforced steel powder. Acta Materialia, 87:377–389, 2015.

[43] Clélia Couchet, Sébastien Y.P. Allain, Guillaume Geandier, Julien Teixeira, Steve Gaudez, Juan Macchi, Mathias Lamari, and Frédéric Bonnet. Recovery of severely deformed ferrite studied by in situ high energy x-ray diffraction. Materials Characterization, 179:111378, 2021.

[44] Akinobu Shibata, Toshio Murakami, Shigekazu Morito, Tadashi Furuhara, and Tadashi Maki. The origin of midrib in lenticular martensite. Materials transactions, 49(6):1242–1248, 2008.

[45] L. C. Chang and H. K. D. H. Bhadeshia. Austenite films in bainitic microstructures. Materials Science and Technology, 11(9):874–882, 1995.

[46] Hong-Seok Yang and HKDH Bhadeshia. Uncertainties in dilatometric determination of martensite start temperature. Materials Science and Technology, 23(5):556–560, 2007.

[47] SMC Van Bohemen. Bainite and martensite start temperature calculated with exponential carbon dependence. Materials Science and Technology, 28(4):487–495, 2012.

[48] David Barbier. Extension of the martensite transformation temperature relation to larger alloying elements and contents. Advanced Engineering Materials, 16(1):122–127, 2014.

[49] Khushboo Rakha, Hossein Beladi, Ilana Timokhina, Xiangyuan Xiong, Saurabh Kabra, Klaus-Dieter Liss, and Peter Hodgson. On low temperature bainite transformation characteristics using in-situ neutron diffraction and atom probe tomography. Materials Science and Engineering: A, 589:303–309, 2014.

[50] Sébastien YP Allain, Steve Gaudez, Guillaume Geandier, Frédéric Danoix, Michel Soler, and Mohamed Gouné. Carbon heterogeneities in austenite during quenching & partitioning (q&p) process revealed by in situ high energy x-ray diffraction (hexrd) experiments. Scripta Materialia, 181:108–114, 2020.

[51] Hossein Beladi, Ilana B Timokhina, Peter D Hodgson, and Yoshitaka Adachi. Characterization of nano-structured bainitic steel. In International Journal of Modern Physics: Conference Series, volume 5, pages 1–8. World Scientific, 2012.

[52] M Dehmas, F Bruneseaux, G Geandier, E Gautier, B Appolaire, S Denis, B Denand, A Settefrati, A Mauro, M Peel, et al. Apport de la diffraction synchrotron à l'étude de la transformation martensitique dans les aciers. Matériaux & Techniques, 97:61–69, 2009.

[53] Sébastien Yves Pierre Allain, Steve Gaudez, Guillaume Geandier, Jean-Christophe Hell, Mohamed Gouné, Frédéric Danoix, Michel Soler, Samy Aoued, and Angeline Poulon-Quintin. Internal stresses and carbon enrichment in austenite of quenching and partitioning steels from high energy x-ray diffraction experiments. Materials Science and Engineering: A, 710:245–250, 2018.

[54] Nina Gunkelmann, Hassel Ledbetter, and Herbert M Urbassek. Experimental and atomistic study of the elastic properties of α' fe–c martensite. Acta materialia, 60(12):4901–4907, 2012.

[55] SMC Van Bohemen. The nonlinear lattice expansion of iron alloys in the range 100–1600 k. Scripta Materialia, 69(4):315–318, 2013.

[56] Matteo Villa, Karen Pantleon, and Marcel AJ Somers. Evolution of compressive strains in retained austenite during sub-zero celsius martensite formation and tempering. Acta materialia, 65:383–392, 2014.

[57] Nobuo Nakada, Yuji Ishibashi, Toshihiro Tsuchiyama, and Setsuo Takaki. Self-stabilization of untransformed austenite by hydrostatic pressure via martensitic transformation. Acta Materialia, 110:95–102, 2016.

[58] M Villa, F Niessen, and MAJ Somers. In situ investigation of the evolution of lattice strain and stresses in austenite and martensite during quenching and tempering of steel. Metallurgical and Materials Transactions A, 49(1):28–40, 2018.

[59] DJ Dyson. Effect of alloying additions on the lattice parameter of austenite. J. Iron Steel Inst., 208:469–474, 1970.

[60] CP Scott and J Drillet. A study of the carbon distribution in retained austenite. Scripta Materialia, 56(6):489–492, 2007.

[61] SMC Van Bohemen and Lutz Morsdorf. Predicting the ms temperature of steels with a thermodynamic based model including the effect of the prior austenite grain size. Acta Materialia, 125:401–415, 2017.

[62] Daisuke Fukui, Nobuo Nakada, and Susumu Onaka. Internal residual stress originated from bain strain and its effect on hardness in fe–ni martensite. Acta Materialia, 196:660–668, 2020.

[63] E. Nes. Recovery revisited. Acta Metallurgica et Materialia, 43(6):2189–2207, 1995.

[64] G. Ghosh and G.B. Olson. The isotropic shear modulus of multicomponent fe-base solid solutions. Acta Materialia, 50(10):2655–2675, 2002.

[65] Sebastien Allain, Olivier Bouaziz, and Manabu Takahashi. Toward a new interpretation of the mechanical behaviour of as-quenched low alloyed martensitic steels. ISIJ international, 52(4):717–722, 2012.

[66] Francesca G Caballero, Michael K Miller, and C Garcia-Mateo. Carbon supersaturation of ferrite in a nanocrystalline bainitic steel. Acta Materialia, 58(7):2338–2343, 2010.

[67] Rosalia Rementeria, Carlos Capdevila, Ricardo Domínguez-Reyes, Jonathan D Poplawsky, Wei Guo, Esteban Urones-Garrote, Carlos Garcia-Mateo, and Francisca G Caballero. Carbon clustering in low-temperature bainite. Metallurgical and Materials Transactions A, 49(11):5277–5287, 2018.

[68] A Seeger and P Haasen. Density changes of crystals containing dislocations. The Philosophical Magazine: A Journal of Theoretical Experimental and Applied Physics, 3(29):470–475, 1958.

[69] David Kalish and Morris Cohen. Structural changes and strengthening in the strain tempering of martensite. Materials Science and Engineering, 6(3):156–166, 1970.

[70] Guillaume Badinier, Chad W. Sinclair, Sébastien Allain, Frédéric Danoix, and Mohamed Gouné. The Mechanisms of Transformation and Mechanical Behavior of Ferrous Martensite. In Reference Module in Materials Science and Materials Engineering, pages 1–34. Elsevier, 2017.

[71] GV Kurdjumov and AG Khachaturyan. Phenomena of carbon atom redistribution in martensite. Metallurgical Transactions, 3(5):1069–1076, 1972.

[72] LS Kremnev. Effect of doping components on the tetragonality of highly doped low-carbon steel martensite. Technical Physics, 58(9):1288–1290, 2013.

[73] Liu Xiao, Zhong Fan, Zhang Jinxiu, Zhang Mingxing, Kang Mokuang, and Guo Zhenqi. Lattice-parameter variation with carbon content of martensite. i. x-ray-diffraction experimental study. Physical Review B, 52(14):9970, 1995.

[74] Rosalia Rementeria, Jonathan D. Poplawsky, Maria M. Aranda, Wei Guo, Jose A. Jimenez, Carlos Garcia-Mateo, and Francisca G. Caballero. Carbon concentration measurements by atom probe tomography in the ferritic phase of high-silicon steels. Acta Materialia, 125:359–368, 2017.

[75] Guillaume Badinier. The effect of carbon segregation and carbide precipitation on the mechanical response of martensite. PhD thesis, University of British Columbia, 2013.

[76] J Wilde, A Cerezo, and GDW Smith. Three-dimensional atomic-scale mapping of a cottrell atmosphere around a dislocation in iron. Scripta Materialia, 43(1):39–48, 2000.

[77] Francesca G Caballero, Michael K Miller, Suresh S Babu, and C Garcia-Mateo. Atomic scale observations of bainite transformation in a high carbon high silicon steel. Acta Materialia, 55(1):381–390, 2007.

[78] Osamu Waseda, Roberto GA Veiga, Julien Morthomas, Patrice Chantrenne, Charlotte S Becquart, Fabienne Ribeiro, Andrei Jelea, Helio Goldenstein, and Michel Perez. Formation of carbon cottrell atmospheres and their effect on the stress field around an edge dislocation. Scripta Materialia, 129:16–19, 2017.

[79] Bevis Hutchinson, Joacim Hagström, Oskar Karlsson, David Lindell, Malin Tornberg, Fredrik Lindberg, and Mattias Thuvander. Microstructures and hardness of as-quenched martensites (0.1–0.5% c). Acta Materialia, 59(14):5845–5858, 2011.

[80] Samy Aoued. Étude des mécanismes d'enrichissement en carbone de l'austénite dans les aciers duplex Q&P à très haute résistance. PhD thesis, Bordeaux, 2019.

[81] GR Speich. Tempering of low-carbon martensite. Trans Met Soc AIME, 245(12):2553–2564, 1969.

[82] B Soenen, AK De, S Vandeputte, and BC De Cooman. Competition between grain boundary segregation and cottrell atmosphere formation during static strain aging in ultra low carbon bake hardening steels. Acta materialia, 52(12):3483–3492, 2004.

[83] J. Svoboda, G.A. Zickler, E. Kozeschnik, and F.D. Fischer. Kinetics of interstitial segregation in cottrell atmospheres and grain boundaries. Philosophical Magazine Letters, 95(9):458–465, 2015.